Chemical Kinetic Studies Using Ultraviolet Cavity Ring-Down Spectroscopic Detection: Self-Reaction of Ethyl and Ethylperoxy Radicals and the Reaction $O_2 + C_2H_5 \rightarrow C_2H_5O_2$

Dean B. Atkinson[†,‡] and Jeffrey W. Hudgens*

Physical and Chemical Properties Division, Chemical Science and Technology Laboratory, National Institute of Standards and Technology, Gaithersburg, Maryland 20899

Received: January 16, 1997; In Final Form: March 20, 1997[⊗]

A laser photolysis reactor that uses cavity ring-down spectroscopic (CRDS) detection was characterized and used to measure the rate coefficients of three benchmark reactions of known importance to ethane oxidation. At 295 K and approximately 700 Pa (5.5 Torr) total pressure, we obtained the self-reaction rate coefficients of $k = (1.99 \pm 0.44) \times 10^{-11}$ cm^3 molecule^{-1} s^{-1} for $C_2H_5 + C_2H_5$ and $k = (7.26 \pm 2.4) \times 10^{-14}$ cm^3 molecule^{-1} s^{-1} for $C_2H_5O_2 + C_2H_5O_2$. We obtained $k = (2.7 \pm 0.3) \times 10^{-12}$ cm^3 molecule^{-1} s^{-1} for the pseudo-first-order association reaction $O_2 + C_2H_5 + Ar$. We also measured the absorption cross sections of the ethyl radical, $\sigma_{220} = (252 \pm 42) \times 10^{-20}$ cm^2 molecule^{-1} and $\sigma_{222} = (206 \pm 42) \times 10^{-20}$ cm^2 molecule^{-1}. Stated uncertainties are 2σ. The new rate coefficients agree with those obtained previously by other methods. The agreement confirms that ultraviolet CRDS detection is a viable tool for experimental determinations of gas-phase radical−radical and radical−molecule reaction rate coefficients.

Introduction

In recent years investigators have used cavity ring-down spectroscopic (CRDS) detection[1−7] to study vibrational and electronic spectroscopy,[8−21] photochemistry,[18] chemical kinetics,[17,18,22−28] and other processes.[16,29−31] The CRDS measurement is conceptually simple; absorption is derived from the increased decay rate of laser radiation within a stable optical cavity induced by absorbing species. Since its first applications, the specifications required for accurate concentration measurements with CRDS detection have evolved within the archival scientific literature.[1−5] Although previous experimental studies have used the vast improvements in sensitivity and precision offered by CRDS, only one experimental study has investigated the conditions under which concentration measurements by CRDS may achieve the same accuracy as obtained with conventional absorbance methods.[32] This study showed that accurate measurements of species concentrations with CRDS will usually require detailed spectral knowledge of the molecular line shape, the laser, and the resonant cavity.

No studies have validated the use of CRDS detection in chemical kinetics by describing experiments that reproduced well-accepted reaction rate coefficients. Such confirmation is one objective of this study. We have incorporated CRDS detection into a laser photolysis reactor and used the reaction system

$$Cl_2 + h\nu\ (308\ \text{nm}) \rightarrow 2Cl \quad (1)$$

$$Cl + C_2H_6 \rightarrow HCl + C_2H_5 \qquad k = 5.7 \times 10^{-11}\ \text{cm}^3\ \text{molecule}^{-1}\ \text{s}^{-1} \quad (2)$$

$$C_2H_5 + C_2H_5 \rightarrow \text{products} \qquad k_\infty = 1.9 \times 10^{-11}\ \text{cm}^3\ \text{molecule}^{-1}\ \text{s}^{-1} \quad (3)$$

$$C_2H_5 + O_2 \rightarrow C_2H_5O_2 \qquad k_\infty = 8.0 \times 10^{-12}\ \text{cm}^3\ \text{molecule}^{-1}\ \text{s}^{-1} \quad (4)$$

$$C_2H_5O_2 + C_2H_5O_2 \rightarrow \text{products} \qquad k_\infty = 6.8 \times 10^{-14}\ \text{cm}^3\ \text{molecule}^{-1}\ \text{s}^{-1} \quad (5)$$

to measure the rate coefficients of reactions 3−5. This system is attractive for study because ethane oxidation is prototypical of aliphatic hydrocarbon oxidation. The rate constants listed for reactions 2−5 are from ref 33.

This reaction sequence tests the ability of CRDS to measure absolute concentrations of reactive species within an evolving chemical system. The rate coefficients of reactions 3 and 5 appear in pure second order and differ by about 3 orders of magnitude. The rate coefficient of reaction 4 is determined in pseudo-first-order from an ensemble of experiments. The kinetic determinations of reactions 3 and 5 hinge upon absolute concentration measurements of C_2H_5 and $C_2H_5O_2$ radicals. The protocols developed here are applicable to the more difficult problem of cross-reaction kinetics between different radicals.

Reactions 3−5 contain formally termolecular processes, that is, reactions which require collisions to stabilize the reaction adduct. At the pressure range of the present study the rate coefficients of self-reactions 3 and 5 are at the high-pressure limit (k_3, $k_5 \sim k_\infty$), and the rate coefficient of reaction 4 lies between the two pressure limits ($k_0[M] > k_4 < k_\infty$). In flow tubes and flash photolysis reactors several groups have measured reactions 3−5 using ultraviolet absorption and mass spectrometry to detect the products or reactants.[34−49] Where experimental conditions overlap, these data are in agreement. We confined this study to 295 K, but our results expand the total pressure range over which reactions 3 and 5 have been studied. The experimental procedures presented here produced reaction rate coefficients that are in good agreement with those obtained previously by other experimental methods.

Experimental Apparatus and Procedures

Figure 1 diagrams the laser photolysis reactor that uses cavity ring-down absorption detection. The gas mixing system delivers

[†] NIST National Research Council Postdoctoral Associate.
[‡] E-mail: Dean.Atkinson@nist.gov.
* E-mail: Jeffrey.Hudgens@nist.gov. Fax 301-975-3672.
[⊗] Abstract published in *Advance ACS Abstracts,* May 1, 1997.

S1089-5639(97)00240-5

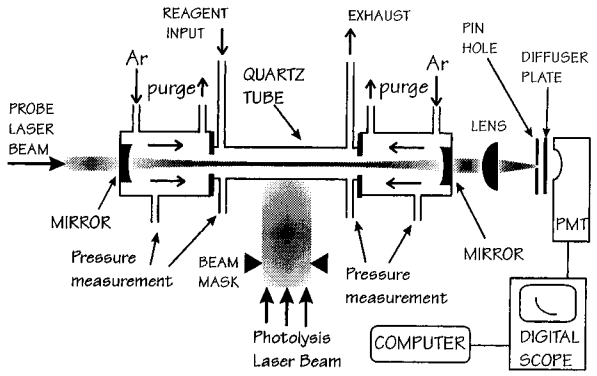

Figure 1. A diagram of the laser photolysis reactor that uses cavity ring-down absorption detection.

a mixture of a buffer (Ar, 99.995%), the photolytic target (10% Cl_2, 99.7%, in He, 99.995%, or neat, commercial grade Cl_2, 99.5%), the radical precursor ethane (research grade, 99.99%, or commercial grade, 99.0%), and other reagents (O_2, 99.6%) to the reactor. Gases of stated purity (Matheson Gas)[50] were used without further purification. The partial pressures of the gases are regulated by mass flow controllers (MKS Model 1259C.) The pumping speed of the main exhaust line (8.3 L/s mechanical pump) is throttled to produce the desired total system pressure and refresh rate. The pressure is measured upstream and downstream of the reaction region using a capacitance diaphragm gauge (MKS Model 220C). In order to protect the dielectric coated mirrors, a counterflow of argon is maintained in the tube extensions as illustrated in the figure. The flow rate of the argon is regulated to minimize mixing of the counterflow and main flow.

These experiments use two lasers. An energy-stabilized excimer laser (Lumonics Model EX700 XeCl 308 nm, 400 mJ/pulse maximum, 20 ns pulse duration) produces the photolysis laser beam. At the output coupler the photolysis laser beam is 5 mm high × 30 mm wide. A pulsed dye laser (Lambda-Physik Model FL 2002; fwhm = 0.2 cm^{-1}, Coumarin 440 and 540A and PTP dyes) pumped by a XeCl excimer laser (Lambda-Physik Model EMG-201-MSC XeCl 308 nm, 300 mJ/pulse, 20 ns pulse width) produces the probe laser beam. To generate light between 210 and 330 nm, the probe laser beam is frequency doubled in BBO or KDP* crystals. To obtain a well-defined spatial profile, the probe beam is propagated into the far field and passed through a 2 mm diameter aperture. The probe beam intensity was <1 mJ cm^{-2} $pulse^{-1}$ at 220 nm and <100 μJ cm^{-2} $pulse^{-1}$ at 270 and 340 nm. A pulse delay generator (Stanford Research Systems Model DG-535), programmed by the data acquisition computer, controls the timing relationship between the photolysis and probe lasers. The temporal uncertainty between the photolysis and probe laser beams is <100 ns.

Three different photolysis arrangements are used. In all arrangements the reaction mixture flows slowly (1−10 m s^{-1}) along a cylindrical quartz tube (16 mm i.d., 1 mm wall), and the photolysis laser beam crosses the quartz tube perpendicular to the flow direction. To achieve the highest power density (and thus radical concentrations), the rectangular beam emitted by the excimer laser is shaped by a cylindrical lens (focal length = 100 mm, 50 mm diameter) so that it irradiates a stripe 7 mm high × 45 mm wide at the center of the quartz reaction tube. To eliminate the less intense, diffuse regions on the beam edges, the photolysis laser beam is defined by a rectangular mask. The power density afforded by this arrangement is sufficient to photolyze approximately 1% of the (1−5) × 10^{16} molecules cm^{-3} concentration of Cl_2 gas present in the flow tube. The 7 × 45 mm photolysis beam was used during measurements of the rapid reaction rates of reaction 4 and during the studies which verified the Beer−Lambert behavior.

Lower initial radical concentrations are generally desirable for kinetics measurements of radical−radical reactions. Since Cl atom production is proportional to the laser beam energy flux, we can reduce the Cl atom concentrations and increase the absorption path length, l_{abs}, by expanding the beam. To prepare a 10 mm high × 75 mm wide stripe, we use a cylindrical lens to shape the photolysis beam. When we allow the photolysis laser beam to propagate ∼4 m beyond the output coupler, it diverges into a uniform 20 mm high × 50 mm wide block. Masks are used to define the beam shape and to eliminate the less intense, diffuse regions on the beam edges. Using a thermal detector masked with a 1 cm diameter aperture, we measure the spatial energy profiles of these beams. The masks are constructed so that the energy at the beam edge does not drop below 90% of the beam center energy. The total energy transmitted by the masked portion of this photolysis beam does not fluctuate by more 10%. When visually examined with a fluorescent card, the masked photolysis beam does not exhibit small-scale intensity structure (i.e., shadows or hot spots) on either the per shot or time-averaged basis. Because the 20 × 50 mm photolysis beam overfills the diameter of the quartz flow tube, this beam profile has the advantage of producing a more uniform density of radicals across the reactor which essentially eliminates the possibility of transient effects originating from radial diffusion. The power density afforded by the two larger beam profiles is sufficient to photolyze approximately 0.1% of the Cl_2 molecules within the reactor. For all Cl_2 partial pressures and photolysis beam dimensions used during this study, Cl_2 absorbs less than 1% of the photolysis beam flux so that we can regard the flow reactor mixtures as optically thin at 308 nm.

After the photolysis laser pulse dissociates the Cl_2 molecules, the chlorine atoms react with the organic precursor (C_2H_6) to form ethyl radicals and HCl (reaction 2). To minimize side reactions and to make the formation rate of the ethyl radicals much greater than other reactions ($t_{1/2}$ ∼ 2 μs), the ethane precursor concentration is kept in large excess over the chlorine atoms. After forming, the ethyl radicals may self-react, react with other radicals, or react with stable species. Partial pressures of the ethyl radicals and their reactants were adjusted to keep the initial reaction half-life between 20 and 1000 μs.

The cavity ring-down detection system (Figure 1) measures absorption along the axis parallel to the flow direction. The stable, near-confocal cavity is constructed from two dielectric-coated mirrors (1000 mm radius of curvature, 25.4 mm diameter) separated by 1.08 m. To permit easy cleaning and replacement, the mirrors are sealed with O-rings in standard vacuum flanges. The mirror flanges, which are attached to metal tube extensions via bellows, are securely held in 76 mm diameter optical mounts, allowing for fine cavity adjustment while maintaining vacuum integrity.

The absorption measurement begins when the probe laser injects a pulse into the cavity through one mirror. The cavity retains the fraction of the laser beam matching the frequency content and spatial profile of the cavity modes. The laser pulse circulates between the mirrors as loss mechanisms (*i.e.*, scattering and absorption, and the leakage through the mirrors) cause each cavity mode to undergo first-order decay. A greatly attenuated laser beam exits through the second cavity mirror. A lens (focal length = 100 mm, 25.4 mm diameter) focuses the output beam through a 1 mm aperture onto a frosted quartz diffuser. An ultraviolet-sensitive photomultiplier tube (PMT)

detects the diffused light. The aperture minimizes interference from scattered photolysis laser light and noise from room light. Because the signal is comprised of many transverse cavity modes, the focusing lens and the diffuser are needed to eliminate signal modulations that may arise from inhomogeneities in the spatial sensitivity function of the PMT.[4,51]

The PMT (Hammamatsu R955AH; 24 × 8 mm, side-window multialkali cathode) is mounted in a base socket (Products for Research PR1405SHRF009) wired for fast response (t_{rise} < 1 ns), low gain (five stages amplification) operation, and is operated at voltages between 500 and 800 V.[52] The unamplified output of the photomultiplier terminates at the 50Ω input of the digital oscilloscope (Lecroy Model 9374; analog bandwidth = 1 GHz, digitizing rate = 5×10^8 samples s^{-1}, full-screen vertical resolution of 8 bits) which records the time evolution of the ring-down signal induced by each probe laser pulse. A PIN photodiode that monitors the probe (CRDS) laser pulse triggers the oscilloscope. To maximize the digital resolution of the oscilloscope, the analog gain of the oscilloscope and the voltage applied to the PMT are adjusted so that the ring-down oscilloscope trace occupies greater than 90% of the vertical display.

Following each probe laser pulse, the digital data are transferred as an integer array to a Pentium computer via the IEEE-488 interface (National Instruments GPIB-AT). The extraction of the decay constant is accomplished using a LabView virtual instrument (National Instruments, Inc.) which truncates the array at 3(1/*e*) times (95% signal decrease, typically 500−2000 data points), subtracts the pre-ring-down base line, converts the array into double-precision floating-point numbers, and fits the ring-down decay to an exponential function of the form

$$I(t) = I_0 e^{-\beta t} \tag{6}$$

where β is the intensity loss rate for the laser pulse in the cavity, I_0 is the initial light intensity of the cavity modes, and t is time. For each laser pulse we calculate a β_i, and the average β is calculated from the linear average over N laser pulses, that is, $\langle\beta\rangle = \sum\beta_i/N$.

The decay rate obtained for an evacuated cavity, β_{empty}, is the summation of all loss mechanisms extant in the cavity. In flash photolysis kinetics experiments the base loss rate against which absorption is measured, β_{base}, also includes any absorption loss contributed by the prephotolysis gas mixture ($\beta_{base} = \beta_{empty} + \beta_{gas}$). Extraction of the fractional intensity loss per pass through the cavity is obtained by multiplying β by the time per pass. The introduction of an absorbing medium into the cavity accelerates the loss rate, β_{abs}. Average absorbance, $\langle A\rangle$, is obtained from the difference between these rates

$$\langle A\rangle = (L/c)(\langle\beta_{abs}\rangle - \langle\beta_{base}\rangle) \tag{7}$$

where L is cavity length and c is the speed of light. The statistical deviation of β_{base} ultimately limits the absolute sensitivity of the absorbance measurement. Assuming Beer−Lambert behavior,

$$\langle A\rangle = nl_{abs}\sigma_\lambda \tag{8}$$

where n is the density of the absorber, σ_λ is the absorption cross section at λ_{CRDS}, and l_{abs} is the absorption pathlength. For the kinetics experiments l_{abs} is defined by the width of the photolysis laser beam.

Figure 2 shows a typical ring-down signal obtained from one laser pulse. For this example the cavity and pinhole are well-aligned (Figure 2a,b). Although the ring-down signal exhibits residual high-frequency intensity modulation (*cf.* Figure 2b), it follows a single-exponential decay function. Figure 2c shows a typical ring-down signal obtained when the cavity is misaligned or the pinhole sits slightly off the axis of the cavity beam. The signal exhibits high-contrast, low-frequency oscillations that originate from beating among the transverse cavity modes. As discussed in other reports,[4,51] beating occurs because misalignments cause incomplete observation of the light exiting the cavity which breaks the orthogonality between corresponding cavity modes. The same effect may also occur when using a detector that has strong gain variation as a function of position across its photoactive surface. A fit of the data in Figure 2c with eq 6 yields a β that has a large residual error.

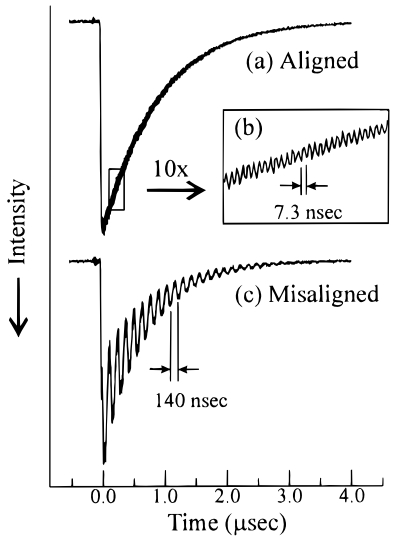

Figure 2. Typical cavity ring-down signals at 270 nm observed in an empty cavity (R = 99.6% mirrors). (a) The ring-down signal observed when the cavity and the exiting pinhole are properly aligned. (b) A temporally magnified (∼10×) portion of the decay showing the small high-frequency beat patterns. (c) The ring-down signal observed when the cavity or the pinhole is misaligned so that part of the beam exiting the cavity is obscured.

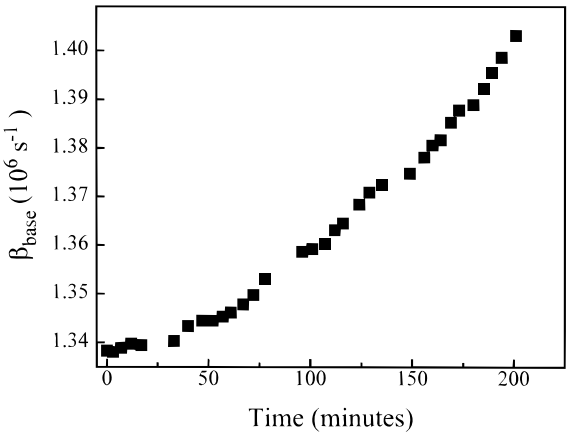

Figure 3. Base loss rate of the cavity ring-down mirrors at 270 nm as a function of time. The argon purge near the mirrors equaled 10% of the total gas flow within the reactor. Although the base loss rate increases with time, cleaning restores the mirrors to their optimum performance levels.

During experiments pollutants deposit on the mirrors and gradually increase their base loss rates. Cleaning restores the mirrors to their optimum performance levels. Figure 3 plots the change in the base loss rate, β_{base}, at 270 nm during a typical experiment that measures the rate coefficient of reaction 5. The flow tube contained a mixture of Ar, chlorine, ethane, and

TABLE 1: Chemical Species, Their Detection Wavelengths, Parameters Observed for Their Detection by CRDS, Absorption Cross Sections, and Theoretical Detection Limits

species detected	λ_{CRDS}, nm	$1/\beta_{empty}$, ns	R^*,[a] %	σ_λ,[b] 10^{20} cm^2 molecule^{-1}	practical detection limit,[c] (molecule-cm^{-3})
Cl_2	340	1333	99.7	23.6[d]	3×10^{12} [e]
$C_2H_5O_2$	265	419	99.1	265[f]	1.2×10^{12}
	270	853	99.6	214[f]	7.5×10^{11}
C_2H_5	220	428	99.2	252 ± 42[g]	1.3×10^{12}
	222	514	99.3	206 ± 42[g]	1.3×10^{12}

[a] Mirror reflectivity efficiency includes transmission, scattering, and diffraction losses. See text. [b] Absorption cross section is in base e. [c] Based on $l_{abs} = 75$ mm unless indicated otherwise. [d] From ref 53. [e] Based on $l_{abs} = 230$ mm. See text. [f] From ref 33. [g] This work.

oxygen and was exposed to a 308 nm photolysis laser every 100 ms. The argon purge near the mirrors equaled 10% of the total gas flow within the reactor. This purge slowed, but did not stop, a gradual increase in the base loss rate. Over the course of 3 h β_{base} increased by 4%. This gradual increase in β_{base} is of the same magnitude as the change in β induced by a single photolysis pulse. To account for increasing base loss rates during kinetics measurements, we measure β_{base} immediately before each measurement of β_{abs}. The average absorbance is calculated using the new $\langle\beta_{base}\rangle$.

During kinetic measurements the concentrations of radicals vs time are obtained by collecting data for a range of delay intervals (e.g., for reaction 3, $t = 0-1000$ μs) between the photolysis and probe laser pulses. To minimize error from long-term system drift, the computer program randomly selects the delay interval and averages the data. Most experiments achieve good signal-to-noise ratios by averaging about 25 absorbance measurements at each delay time. During these studies we ascertained that the flow tube was replenished with fresh reaction mixture for every laser shot by measuring the absorbance at very long reaction times ($t = 200-1000$ ms). These absorbance measurements showed that the faster reactions 3 and 4 exhibit no residual absorptions when the experiments are conducted at 5−10 Hz. The persistence of the ethylperoxy radical required us to reduce the refresh rate of the reactor so that the reacting mixture would not be swept out of the reactor during the kinetic measurement. This limited measurements of reaction 5 to between 2 and 5 Hz.

The features of our experimental apparatus are as follows: (1) The reaction takes place in a well-defined spatial region, which is much larger than the probed volume, minimizing wall contributions. (2) The reaction zone is produced by a uniform photolysis beam. (3) The width of the masked photolysis beam precisely defines the absorbance path length. (4) For experiments that use the 20 × 50 mm photolysis beam, the effects of radial diffusion are minimized.

Results

Characterization of the CRDS Detection System. During this study the concentrations of Cl_2, ethyl radicals, and ethylperoxy radicals were monitored using cavity ring-down detection. For each species Table 1 lists the detection wavelength λ_{CRDS}, the ring-down time at λ_{CRDS} obtained for an empty cavity ($1/\beta_{empty}$) equipped with freshly cleaned mirrors, the reflection efficiency ($R^* = 1 - L/c\langle\beta_{empty}\rangle$) of the mirrors at λ_{CRDS}, the absorption cross section of each chemical species at λ_{CRDS}, and the practical detection limit for each target species. Reflection efficiency, R^*, is the fraction of light that a cavity mirror (mounted in a specific cavity) returns to the cavity modes. Unlike reflectivity, its calculation contains all loss mechanisms, including scattering, diffraction, and transmission. The practical detection limits are derived assuming the absorption cross section at λ_{CRDS}, the photolytically generated 75 mm path length, and that the absorbance measurement has a minimum signal-to-noise ratio of S/N = 3.

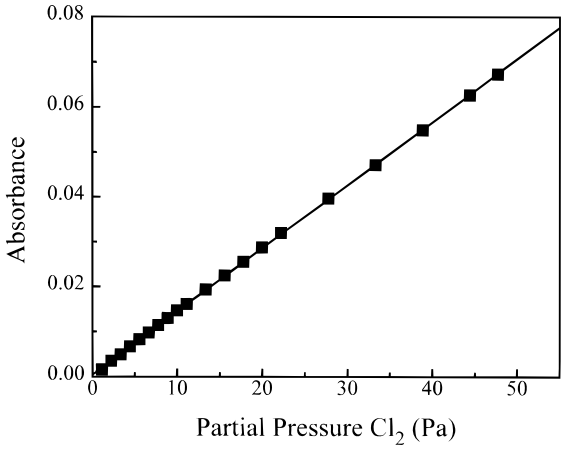

Figure 4. Absorbance vs Cl_2 partial pressure in the flow reactor measured by cavity ring-down detection at 340 nm.

Near each respective λ_{CRDS} previous spectroscopic investigations of Cl_2,[53] C_2H_5,[54] and $C_2H_5O_2$[39] have found that radiationless processes (*e.g.*, dissociation, geometry changes, predissociation, intersystem crossing) homogeneously broaden the rotational lines into a continuous spectrum. This broadening causes the absorption cross sections at each λ_{CRDS} to remain constant across the probe laser line width. In a ring-down cavity a uniform absorption constant will cause the spectrum of populated cavity modes to exhibit identical decay rates. Therefore, absorbance at λ_{CRDS}, obtained from cavity ring-down rates, should change linearly with species concentration.[2,32] We have conducted several tests to verify that the absorbance measurements within the reactor conform to Beer−Lambert behavior, that is, that absorbance changes in proportion to the species concentration, path length, and absorption cross section, σ_λ.

Figure 4 plots the absorbance at 340 nm as a function of Cl_2 density in the flow tube in a large excess of Ar. Since Cl_2 is a stable species, its density profile is determined by the flow pattern along the length of the cavity; thus, the absorbance path length is not precisely defined. During this experiment we kept the path length constant by keeping the flow conditions essentially unchanged as the flow rate of Cl_2 was varied. Assuming that the majority of the Cl_2 is confined within the quartz flow tube of the reactor (Figure 1), the absorption path length should be $l_{abs} = 230$ mm, yielding an absorption cross section of $\sigma_{340} = 23.6 \times 10^{-20}$ cm^2 molecule^{-1}, which is in excellent agreement with the recommended value of $\sigma_{340} = 23.5 \times 10^{-20}$ cm^2 molecule^{-1}.[53] We note that the minimum absorbance plotted in Figure 4 does not correspond to the instrumental detection limit, which is approximately 3×10^{12} molecule cm^{-3} (Table 1). Over the broad range measured (43×), Figure 4 shows that absorbance is a linear function of Cl_2 density.

Figure 5 plots the derived peak $C_2H_5O_2$ radical density as a function of Cl_2 partial pressure in the reaction mixture. The $C_2H_5O_2$ radicals form via the reaction sequence (1), (2), and (4). Because the photolysis laser pulse energy was held constant and the sample was optically thin at the photolysis wavelength, the $C_2H_5O_2$ radical density is proportional to the amount of Cl_2 added to the otherwise constant mixture of ethane (26.6 Pa), oxygen (46.6 Pa), and argon (700 Pa). The $C_2H_5O_2$ radical

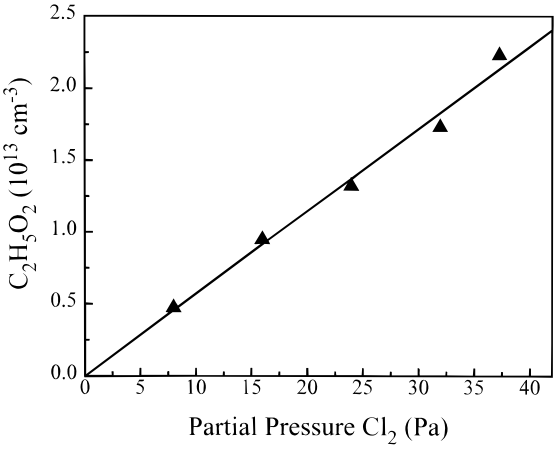

Figure 5. Derived peak $C_2H_5O_2$ radical density as a function of Cl_2 partial pressure in the reaction mixture.

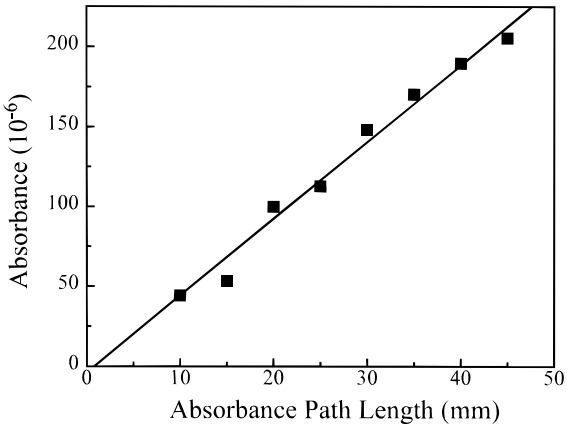

Figure 6. Peak absorbance of $C_2H_5O_2$ at 270 nm as a function of absorbance path length.

density is calculated from the absorbance observed at 270 nm using σ_{270} for $C_2H_5O_2$ and a 45 mm absorption path length. The linear response of $C_2H_5O_2$ radical absorbance to Cl_2 density is a demonstration of proper Beer−Lambert behavior. In separate experiments we photolyzed mixtures containing no O_2 and found that the peak C_2H_5 absorbance at 220 nm as a function of Cl_2 density also produced a linear plot, similar to Figure 5.

Figure 6 shows the peak absorbance of $C_2H_5O_2$ at 270 nm as a function of absorption path length, l_{abs}. During these experiments the total energies of the photolysis laser and the flow conditions were held constant. The flow reactor mixture contained Cl_2 (3.33 Pa), ethane (26.6 Pa), oxygen (46.6 Pa), He (29 Pa), and argon (700 Pa). The absorbance path length was changed by obscuring portions of the photolysis laser beam along the cavity axis. As required for Beer−Lambert behavior, absorbance is linearly proportional to the irradiated path length. This linear behavior also demonstrates that the photolysis laser beam energy profile is very uniform, in accord with the photolysis beam profile measurements. A separate investigation of peak absorbance of $C_2H_5O_2$ at 270 nm as a function of photolysis laser pulse energy also showed linear behavior. For these experiments the photolysis energy was changed by varying the laser discharge voltage while keeping the irradiated path length and flow conditions constant.

Determination of Absorption Cross Sections for Ethyl Radicals. The published absorption cross sections for the ethyl radical[44,54] are only expected to be quantitative at the absorption maxima. The spectrum of the ethyl radical exhibits two broad absorption features, one centered near 205 nm and the other centered near 245 nm. During the kinetic studies we measured ethyl radical concentrations at 220 nm which lies on a shoulder of the 205 nm absorption band. The absorption spectrum of the ethylperoxy radical is a featureless band extending between 200 and 290 nm.[35,36,39,44]

We remeasured the absorption cross section of the ethyl radicals at 220 nm, σ_{220}, by direct comparison with the known values of σ_{220} for the ethylperoxy radical. First, the peak absorbance at 220 nm was measured for a photolyzed mixture of Cl_2, He, and ethane. Then, to convert all ethyl radicals into ethylperoxy radicals (reaction 4), a stoichiometric excess of O_2 was added to the flow tube mixture, and the peak absorbance at 220 nm was measured again. The peak absorbance observed for each experiment corresponds to the same concentration of ethyl and ethylperoxy radicals, respectively. Three separate measurements found the ratio of peak absorbances to be $[C_2H_5/C_2H_5O_2] = 0.85 \pm 0.05$, which gives a cross section of $\sigma_{220} = (252 \pm 42) \times 10^{-20}$ cm^2 molecule^{-1}, using the recommended cross section at 220 nm for the ethylperoxy radical.[33] We also determined the absorption cross section at 222 nm, $\sigma_{222} = (206 \pm 42) \times 10^{-20}$ cm^2 molecule^{-1}, from the ratio of peak absorbances of ethyl radical at 220 and 222 nm under identical reaction conditions. The lower absorption cross section at 222 nm agrees qualitatively with the published spectra.[44,54] The uncertainty for our cross section measurement represents the error contributions in our relative absorption measurement and the reported uncertainty of the ethylperoxy cross section.

Although it is less accurate, we also experimentally corroborated our σ_{220} of ethyl radical by measuring the Cl_2 absorbance decrease at 340 nm due to 308 nm photolysis. The derived cross sections from these measurements agreed with those derived by comparison to the ethylperoxy absorbance within the experimental uncertainty. Using σ_{308} for Cl_2 and the measured photon flux, the density of Cl atoms and the subsequent densities of ethyl and ethylperoxy radicals were also estimated. These densities were in accord with those derived from absorbance measurements at 220 and 270 nm.

Kinetics Measurements. The self-reaction of ethyl radicals, reaction 3, was studied at room temperature with the third body mainly consisting of Ar ($T = 295$ K, $P_{total} \sim 750$ Pa (5.6 Torr)). The kinetic data were fit to the simple second-order form

$$1/A(t) = 1/A_0 + 2k_{bimolecular}t/\sigma_\lambda l_{abs} \quad (9)$$

where $A(t)$ is the absorbance at time t, A_0 is the initial absorbance, k is the observed bimolecular rate coefficient, t is the time, σ_λ is the absorption cross section at λ_{CRDS}, and l_{abs} is the absorption path length induced by the photolysis laser beam. The factor of 2 arises from the definition of $k_{bimolecular}$. Figure 7 displays a typical second-order rate coefficient determination for k_3. The points represent the averaged concentration measurements of C_2H_5 radicals (obtained from the ring-down absorbance) as a function of time. The solid curve shows the fit of these data to eq 9. The variation of the derived second-order rate coefficient of reaction 3, k_3, as functions of Cl_2 concentration, photolysis energy and path length, and total pressure was investigated. To rule out contributions from a second interfering absorber, these experiments were repeated at 222 nm. Table 2 summarizes all results. Because k_3 does not vary systematically with any of the experimental parameters, we conclude that the measured rate coefficient represents the true rate coefficient.

Under these reaction conditions, ethyl radicals react rapidly with molecular chlorine:[45]

$$C_2H_5 + Cl_2 \rightarrow C_2H_5Cl + Cl$$
$$k = 8.8 \times 10^{-12} \text{ cm}^3 \text{ molecule}^{-1} \text{ s}^{-1} \quad (10)$$

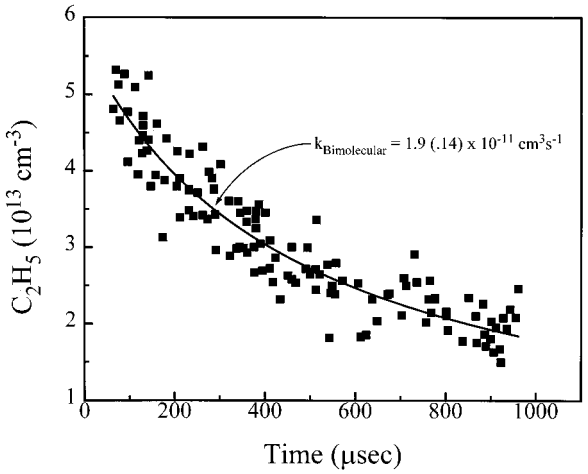

Figure 7. Kinetic plot of the self-reaction of ethyl radicals. The absolute density of C_2H_5 radicals vs time was measured by cavity ring-down absorbance at 220 nm. The solid curve shows the fit of these data.

TABLE 2: Kinetic Results for Reaction 3, $C_2H_5 + C_2H_5$, at 295 K between 637 and 1059 Pa Total Pressure (Ar)

partial press. Cl_2, Pa	photolysis power, mJ/pulse	total press., Pa	$k_{bimolecular}$, 10^{-11} cm^3 $molecule^{-1}$ s^{-1}
47.7	200[a]	774	1.8
47.7	200[a]	774	1.8
21.8	200[a]	773	2.3
39.2	200[a]	1059	1.7
10.9	200[a]	760	1.8
32.7	200[a]	787	2.2
41.8	200[b]	730	2.5
10.5	200[b]	693	1.9
20.9	200[b]	706	1.9
31.4	200[b]	718	2.1
52.3	200[b]	742	2.0
23.5	300[b]	637	2.0[c]
23.5	300[b]	637	1.9[c,d]

[a] This experiment was conducted using a 10 mm high × 75 mm wide photolysis beam. [b] This experiment was conducted using a 20 mm high × 50 mm wide photolysis beam. [c] Commercial grade ethane was used for these measurements; only the first 200 μs of data were used in the determination of k because of O_2 contamination which caused strong curvature in the kinetic plots beyond this time. [d] For this measurement λ_{CRDS} = 222 nm.

The chlorine atom produced by reaction 10 can rapidly regenerate an ethyl radical by reaction with ethane (reaction 2). If the combination of reactions 2 and 10 does not deplete the ethane concentration significantly, these reactions comprise a null cycle that should not distort measurement of k_3. For this reason we held the ethane concentration in at least 2-fold excess over the chlorine concentration.

The association reaction of ethyl radicals with O_2 to form ethylperoxy radicals (reaction 4) was studied in pseudo-first-order with excess oxygen at 295 K. The reaction mixture consisted of ethane (26.6 Pa), Cl_2 (3.33 Pa), O_2 (between 5.3 and 58.5 Pa), and a balance of argon to maintain a total pressure of 730 ± 24 Pa (~5.5 ± 0.2 Torr). Because the subsequent second-order kinetic decay (reaction 5) of the ethylperoxy radical is slow relative to reaction 4, the data treatment was straightforward. The growth of ethylperoxy absorbance at 270 nm was fit to a simple exponential function ($\ln(1 - A(t)/A_{max}) = -k_{obs}t$), allowing extraction of the pseudo-first-order rate coefficient, k_{obs}. Figure 8 displays the pseudo-first-order growths of the $C_2H_5O_2$ radical concentration as a function of time for two O_2 partial pressures. Each solid line shows the fit of the data that extracts a k_{obs} for each partial pressure of O_2. Table 3

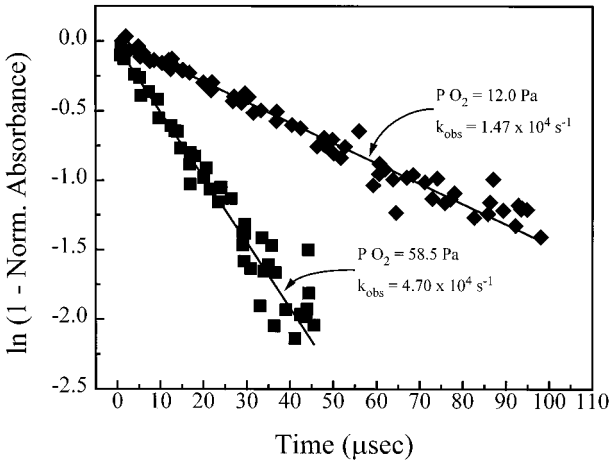

Figure 8. Two pseudo-first-order plots for the growth of ethylperoxy radical concentration at two concentrations of excess oxygen. The growth is modeled as explained in the text. The solid lines represent the derived observed rate coefficients, k_{obs}.

TABLE 3: Summary of Data Used To Derive the Bimolecular Rate Coefficient for Reaction 4, k_4, at 295 K and an Average Pressure of 730 Pa[a]

partial press. O_2, Pa	k_{obs}, 10^4 s^{-1}	total press.,[b] Pa	partial press. O_2, Pa	k_{obs}, 10^4 s^{-1}	total press.,[b] Pa
5.32	0.96 ± 0.24	706	34.6	2.78 ± 0.96	735
12.0	1.47 ± 0.31	713	47.9	4.13 ± 1.3	749
23.3	1.99 ± 0.50	724	58.5	4.70 ± 1.7	759

[a] Derived bimolecular rate coefficient: $k_4 = (2.7 \pm 0.3) \times 10^{-12}$ cm^3 $molecule^{-1}$ s^{-1}. [b] Mostly argon.

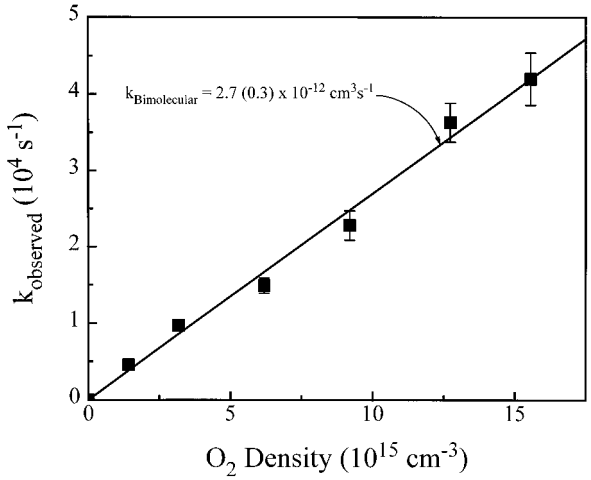

Figure 9. Extraction of the bimolecular rate coefficient for reaction 4, k_4, at 295 K and pressures near 730 Pa (Table 3). The error bars on the observed rate coefficients represent twice the standard error in the derived slopes.

summarizes the ensemble of extracted k_{obs} for several O_2 partial pressures. Figure 9 shows the plot of k_{obs} vs O_2 density from which the bimolecular rate coefficient for reaction 4, k_4, is obtained.

The self-reaction rate coefficient of ethylperoxy radicals (reaction 5), k_5, was measured in second order at 295 K in an excess of argon at 750 ± 100 Pa (5.5 ± 0.75 Torr) total pressure. The absolute concentration of $C_2H_5O_2$ was determined by cavity ring-down absorbance using the published absorption cross sections ($\sigma_{270} = 214 \times 10^{-20}$ cm^2 $molecule^{-1}$ and $\sigma_{265} = 265 \times 10^{-20}$ cm^2 $molecule^{-1}$).[33] Figure 10 shows an example of the observed kinetic decay of ethylperoxy radical absorbance vs time. The solid line is the second-order fit which was used

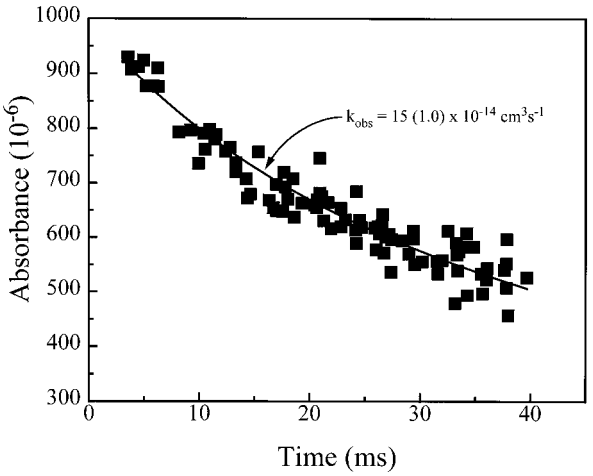

Figure 10. Single determination of the ethylperoxy radical self-reaction (reaction 5) rate coefficient, k_5, at 295 K and 674 Pa. The quoted error (in parentheses) is the twice the standard error in the slope of inverse absorbance vs time.

TABLE 4: Kinetic Results for Reaction 5, $C_2H_5O_2 + C_2H_5O_2$, at 295 K between 674 and 841 Pa Total Pressure (Ar)

partial press. Cl_2,[a] Pa	λ_{CRDS}, nm	photolysis power,[b] mJ/pulse	total press., Pa	$k_{observed}$, 10^{-14} cm^3 $molecule^{-1}$ s^{-1}
56.1	270	200	841	11.0
56.1	270	190	840	9.7
56.1	270	330	841	10.5
56.1	270	400	841	9.7
56.1	270	300	840	10.2
28.1	270	300	811	9.8
28.1[c]	270	300	783	12.0
50.7	270	300	740	11
32.7	270	300	692	16
24.5	265	300	682	12
32.7	265	300	689	13
16.4	265	300	674	15
32.7	265	300	692	13
32.7[d]	265	300	692	14

[a] The flow reactor gas mixture contained ethane (100 Pa) and O_2 (53 pA) unless noted otherwise. [b] These experiments were conducted using a 20 mm high × 50 mm wide photolysis beam. [c] The ethane concentration was reduced to 50 Pa. [d] The repetition rate of the experiment was slowed from 5 to 2 Hz.

to extract the observed bimolecular rate coefficient, k_{obs}. Again, the rate coefficient was measured at two wavelengths at several molecular chlorine concentrations, total pressures, and photolysis energies. Table 4 summarizes these results. As expected, the derived reaction rate coefficient is invariant with experimental conditions.

Reaction 5 proceeds via two major channels

$$C_2H_5O_2 + C_2H_5O_2 \rightarrow 2C_2H_5O + O_2 \quad (5a)$$

$$\rightarrow C_2H_5OH + CH_3CHO + O_2 \quad (5b)$$

which account for about 60 and 40% of the products, respectively.[33] The ethoxy radical formed in reaction 5a then reacts with oxygen to form the hydroperoxy radical, which rapidly removes an ethylperoxy radical:

$$C_2H_5O + O_2 \rightarrow CH_3CHO + HO_2 \quad (11)$$

$$HO_2 + C_2H_5O_2 \rightarrow \text{products} \quad (12)$$

Under our experimental conditions reactions 11 and 12 are rapid with respect to reaction 5. Weak absorption at 270 nm by CH_3CHO[55] will increase k_5 by less than 1% and is ignored in this analysis. In experiments that monitor ethylperoxy radical concentration, reactions 11 and 12 accelerate the observed loss rate of ethylperoxy radical by 70% so that $k_{obs} = 1.7k_5$. Following the conventional treatment,[33] we have multiplied our observed rate coefficients (Table 4) by 0.6 to derive the bimolecular self-reaction rate coefficient, k_5. Since C_2H_5O and HO_2 radicals have negligible absorbance at 270 nm,[34] this treatment is appropriate.

Error Analysis. The (2σ) uncertainties of the rate coefficients, k_3, k_4, and k_5 were statistically derived from the kinetic data. Because rate coefficients k_3 and k_5 showed no dependence upon total pressure, their uncertainties were computed from the complete data sets in Table 2 and 4, respectively. The stated uncertainty of k_4 at 730 Pa (5.5 Torr) represents twice the standard error of the slope in the linear fit of k_{obs} vs O_2 density (Figure 9).

For measurements of k_3 the scatter of the kinetic data is approximately ±10%. Most of this scatter originates from fluctuation of the photolytic production of chlorine atoms. The fluctuation in the photolysis laser intensity is about 10% of the average power. The high quality of the flow measurement and control system limits fluctuations of the Cl_2 partial pressure to ~2% (<1% per flow meter, three or four flow meters total).

For the measurements of k_4 and k_5, absorption by Cl_2 at 270 nm interferes with the cavity ring-down measurement and effectively doubles the scatter in the kinetic data. During these experiments absorption by Cl_2 at 270 nm accounts for about half of the base loss ($\beta_{base} \sim \beta_{empty} + \beta_{Cl_2}$). The 2% fluctuation in Cl_2 density induces an approximately 1% deviation in β_{base}. Absorption by ethylperoxy radicals increases the cavity loss rate by only 10%; hence, the 1% deviation in β_{base} increases the fluctuation in absorbance by an additional 10%. An improvement is expected by selecting a λ_{CRDS} that is absorbed less strongly by Cl_2. Indeed, the statistical deviations of the absorbance measurements at $\lambda_{CRDS} = 265$ nm are somewhat smaller than at $\lambda_{CRDS} = 270$ nm, despite the decreased mirror reflectivity at 265 nm (Table 1). The measured mean value for the bimolecular rate coefficient (Table 4) is unaffected by this change in λ_{CRDS}, as expected.

We may place limits on absolute uncertainties introduced by systematic errors. During measurements of k_3, contaminants in the reaction mixture cause the kinetic decay to deviate from second-order behavior. The trace of O_2, present in the commercial grade chlorine, converts a small fraction of the initial ethyl radical population into ethylperoxy radicals (reaction 4) which absorb very strongly at 220 nm.[33] At longer reaction times absorption by comparatively inert ethylperoxy radical density results a constant nonzero absorption. This non-second-order behavior in the absorption decay ultimately limits the reaction time available for determination of k_3 to about 1 ms, slightly greater than one 1/e decay time for reaction 3 at our experimental conditions. During determinations of k_3 and k_5 we discarded the first 10 μs of the data which showed very rapid non-second-order kinetic decay. We attribute the rapid decay to a second impurity in the chlorine. For example, trace amounts of NO could produce such behavior. The maximum contribution to the absolute error in k_3 due to these effects is estimated at 10%. These effects should not degrade the determinations of k_4 and k_5.

For measurements of k_5 where the reaction time becomes very large, longitudinal diffusion decreases the ethylperoxy radical density and effectively lengthens l_{abs}. These changes offset each other and mask the effects of longitudinal diffusion. However,

TABLE 5: Summary of Reaction Rate Coefficients at 298 K Determined during This Study and by Previous Studies Using Other Methods

reaction rate coeff	total press., Pa	rate coeff., cm^3 $molecule^{-1}$ s^{-1}	technique
$C_2H_5 + C_2H_5$ (k_3)[a]	637−1059	$(1.99 \pm 0.44) \times 10^{-11}$	this work
	20 000−93 000	$(1.69 \pm 0.2) \times 10^{-11}$	molecular modulation/UV absorption[47]
	76 800−78 100	$(1.86 \pm 0.3) \times 10^{-11}$	molecular modulation/UV absorption[46]
	6100	$(2.32 \pm 0.45) \times 10^{-11}$	flash photolysis/UV absorption[40]
$C_2H_5 + O_2 \rightarrow C_2H_5O_2$ (k_4)	706−759 (Ar)	$(2.7 \pm 0.3) \times 10^{-12}$	this work
	491 (He)	2.88×10^{-12} [b,c]	laser photolysis/mass spectrometry[49]
	878 (He)	2.83×10^{-12} [b,c]	laser photolysis/mass spectrometry[42]
	758 (He)	$(2.87 \pm 0.22) \times 10^{-12}$ [c]	discharge flow/mass spectrometry[48]
$C_2H_5O_2 + C_2H_5O_2$ (k_5)[a]	674−841	$(7.3 \pm 2.4) \times 10^{-14}$	this work
	100 000	$(8.2 \pm 0.8) \times 10^{-14}$	flash photolysis/UV absorption[39]
	8000−20000	$(6.6 \pm 0.7) \times 10^{-14}$ [d]	molecular modulation/UV absorption[36]
	3300−53 200	$(5.92 \pm 0.44) \times 10^{-14}$	flash photolysis/UV absorption[34]
	3600−100 000	$(7.80 \pm 0.96) \times 10^{-14}$ [d]	molecular modulation/UV absorption[38]
	55 900−100 000	$(5.69 \pm 0.77) \times 10^{-14}$ [d]	molecular modulation/UV absorption[37]
	77 000−90 000	$(5.98 \pm 0.83) \times 10^{-14}$ [d]	flash photolysis/UV absorption[35]

[a] No systematic variation of the bimolecular rate coefficient with total pressure was observed in this study. [b] No uncertainties quoted. [c] Rate coefficient adjusted to account for reaction 13. See text. [d] The value quoted here represents the application of the factor 0.6 to the observed self-interaction rate coefficient reported by the authors.

the diminished radical density also reduces the observed self-reaction rate coefficient, k_{obs}. At the pressures used during this investigation, one-dimensional modeling of longitudinal diffusion predicts that the half-life for diffusional losses is ∼300 ms.[56] Reactive losses will lengthen this half-life further. The time scale of our measurement of k_5 is typically 40 ms, substantially shorter than the diffusional half-life. Thus, the effects of longitudinal diffusion may lead to a slight underestimation of the reaction rate coefficient, k_5; however, this underestimation should not exceed 5%.

Discussion

Table 5 presents the reaction rate coefficients k_3, k_4, and k_5 determined near 295 K by this investigation and also lists determinations by other well-established techniques. The rate coefficients of this work lie in close agreement to the previous determinations. The pressure range of this study does not overlap that of previous studies of reactions 3 and 5. However, at 295 K $k_{bimolecular}$ is not expected to show pressure dependence above ∼100 Pa for large polyatomic reactants.[57] This study and prior investigations of reactions 3 and 5 have observed no pressure dependence in the rate coefficients, $k_{bimolecular}$. Thus, k_3 and k_5 are approximations of k_∞ for the respective reactions.

Between 100 and 1000 Pa the bimolecular rate coefficient of reaction 4 exhibits pressure dependence. Because they encompass our pressure range, the studies employing mass spectrometric detection offer the best opportunity for comparison with the present results. The caveat implicit with this comparison is that mass spectrometer measurements observe the disappearance of ethyl radical, which includes the reaction channel

$$C_2H_5 + O_2 \rightarrow C_2H_4 + HO_2 \qquad (13)$$

Under the low-pressure conditions of these studies reaction 13 accounts for 10% of the reactivity for $C_2H_5 + O_2$.[48] Thus, to extract k_4 for comparison with the current CRDS results, the rate coefficients quoted in the mass spectrometry studies[42,48,49] should be reduced by 10%. The k_4 obtained by the present CRDS study lies in good agreement with these adjusted mass spectrometric results. In this case, reaction 4 is in the falloff region between the low- and high-pressure limits, $k_0 = 1.5 \times 10^{-28}$ cm^6 $molecule^{-1}$ s^{-1} and $k_4 = 8 \times 10^{-12}$ cm^3 $molecule^{-1}$ s^{-1}.[33]

This study confirms that ultraviolet CRDS detection is a viable tool for experimental determinations of gas-phase radical−radical and radical−molecule reaction rate coefficients. For selected laser wavelengths linear Beer−Lambert behaviors were established for Cl_2, C_2H_5, and $C_2H_5O_2$, demonstrating the utility and reliability of the technique as a simple concentration monitor. The rate coefficients measured with CRDS detection are found to agree well with those obtained by well-established methods.

Thus far, few CRDS studies have used the ultraviolet spectrum, perhaps because many of the molecular continuum spectra in this region are relatively featureless or perhaps because the poor reflectivities of UV mirrors limit the theoretical sensitivity of CRDS detection. However, these unattractive features offer advantages to kineticists. Linear Beer−Lambert CRDS behavior is more easily achieved when using a molecular transition that is homogeneously broadened. Although the poor reflectivities of available UV mirrors limit the ultimate sensitivity of CRDS, low-reflectivity mirrors also produce short ring-down times which improve the time resolution of concentration measurements. Even when limited by mirrors of modest reflection efficiency (Table 1), the detection limits of CRDS in the UV suggest that they are substantial improvements over previous absorption methods. For comparison, with CRDS detection we have measured the rate coefficients of reaction 3 at C_2H_5 concentrations of 10^{12} molecules cm^{-3} with an absorbance path length (l_{abs}) that is an order of magnitude shorter than used previously.

The enhanced sensitivity of cavity ring-down absorption measurements will facilitate the study of radical−radical cross reactions. Since CRDS detection can follow the concentrations of the radicals over a large dynamic range, self-reaction rates are more easily separated from a cross-reaction rate. As demonstrated here, CRDS enables accurate radical−radical reaction rate determinations using low radical concentrations and a short reaction zone. It is easier to produce and to measure uniform radical production in such small systems. Furthermore, the effects of finite absorption of light on the reactivity of these species can now be ruled out, since the assumption of optically thin absorption is well satisfied in these measurements.

This report also contains new results which extend the known pressure range for reactions 3 and 5. At 295 K and 700 Pa the assumption of saturated termolecular behavior still applies; however, in extending the temperature range higher, the onset of falloff behavior should become evident at the relatively low pressures available to this technique. This emphasizes an important aspect of the current experimental design, it is quite

versatile as regards total pressure, temperature, and magnitude of rate coefficient. The pressure in the reactor can easily be increased above atmospheric pressure without significant changes in the apparatus. Modifications to the apparatus are being made to allow the variation of temperature to between 250 and 600 K. The current results demonstrate the utility of the method over nearly 3 orders of magnitude in the measured rate coefficient.

References and Notes

(1) O'Keefe, A.; Deacon, D. A. G. *Rev. Sci. Instrum.* **1988**, *59*, 2544.
(2) Zalicki, P.; Zare, R. N. *J. Chem. Phys.* **1995**, *102*, 2708.
(3) Scherer, J. J.; Voelkel, D.; Rakestraw, D. J.; Paul, J. B.; Collier, C. P.; Saykally, R. J.; O'Keefe, A. *Chem. Phys. Lett.* **1995**, *245*, 273.
(4) Hodges, J. T.; Looney, J. P.; van Zee, R. D. *J. Chem. Phys.* **1996**, *105*, 10278.
(5) Lehmann, K. K.; Romanini, D. *J. Chem. Phys.* **1996**, *105*, 10263.
(6) Martin, J.; Paldus, B. A.; Zalicki, P.; Wahl, E. H.; Owano, T. G.; Harris, J. S., Jr.; Kruger, C. H.; Zare, R. N. *Chem. Phys. Lett.* **1996**, *258*, 63.
(7) Engeln, R.; Meijer, G. *Rev. Sci. Instrum.* **1996**, *67*, 2708.
(8) Romanini, D.; Lehmann, K. K. *J. Chem. Phys.* **1993**, *99*, 6287.
(9) Romanini, D.; Lehmann, K. K. *J. Chem. Phys.* **1994**, *102*, 633.
(10) Jongma, R. T.; Boogaarts, M. G. H.; Meijer, G. *J. Mol. Spectrosc.* **1994**, *165*, 303.
(11) Lehmann, K. K.; Romanini, D. *J. Chem. Phys.* **1993**, *99*, 6287.
(12) O'Keefe, A.; Scherer, J. J.; Cooksy, A. L.; Sheeks, R.; Heath, J.; Saykally, R. J. *Chem. Phys. Lett.* **1990**, *172*, 214.
(13) Jongma, R. T. *Can. J. Phys.* **1994**, *72*, 1109.
(14) Scherer, J. J.; Paul, J. B.; Collier, C. P.; Saykally, R. J. *J. Chem. Phys.* **1995**, *102*, 5190.
(15) Jongma, R. T.; Boogaarts, M. G. H.; Holleman, I.; Meijer, G. *Rev. Sci. Instrum.* **1995**, *66*, 2821.
(16) Zalicki, P.; Ma, Y.; Zare, R. N.; Wahl, E. H.; Dadamio, J. R.; Owano, T. G.; Kruger, C. H. *Chem. Phys. Lett.* **1995**, *234*, 269.
(17) Zhu, L.; Johnson, G. *J. Phys. Chem.* **1995**, *99*, 15114.
(18) Zhu, L.; Kellis, D.; Ding, C.-F. *Chem. Phys. Lett.* **1996**, *257*, 487.
(19) Pearson, J.; Orr-Ewing, A. J.; Ashfold, M. N. R.; Dixon, R. N. *J. Chem. Soc., Faraday Trans.* **1996**, *92*, 1283.
(20) Pearson, J.; Orr-Ewing, A. J.; Ashfold, M. N. R.; Dixon, R. N. *J. Chem. Phys.*, in press.
(21) Scherer, J. J.; Paul, J. B.; O'Keefe, A.; Saykally, R. J. *Chem. Rev.* **1997**, *97*, 25.
(22) Lin, M. C.; Yu, T. *Int. J. Chem. Kinet.* **1993**, *25*, 875.
(23) Yu, T.; Lin, M. C. *J. Am. Chem. Soc.* **1993**, *115*, 4371.
(24) Yu, T.; Lin, M. C. *Int. J. Chem. Kinet.* **1994**, *26*, 771.
(25) Yu, T.; Lin, M. C.; Melius, C. F. *Int. J. Chem. Kinet.* **1994**, *26*, 1095.
(26) Yu, T.; Lin, M. C. *J. Phys. Chem.* **1994**, *98*, 9697.
(27) Yu, T.; Lin, M. C. *J. Phys. Chem.* **1994**, *98*, 2105.
(28) Yu, T.; Lin, M. C. *J. Phys. Chem.* **1995**, *99*, 8599.
(29) Bernard, D. J.; Winker, B. K. *J. Appl. Phys.* **1991**, *69*, 2805.
(30) Meijer, G.; Boogaarts, M. G. H.; Jongma, R. T.; Parker, D. H.; Wodtke, A. M. *Chem. Phys. Lett.* **1994**, *217*, 112.
(31) Zalicki, P.; Ma, Y.; Zare, R. N.; Wahl, E. H.; Owano, T. G.; Kruger, C. H. *Appl. Phys. Lett.* **1995**, *67*, 144.
(32) Hodges, J. T.; Looney, J. P.; van Zee, R. D. *Appl. Opt.* **1996**, *35*, 4112.
(33) DeMore, W. B.; Sander, S. P.; Golden, D. M.; Hampson, R. F.; Kurylo, M. J.; Howard, C. J.; Ravishankara, A. R.; Kolb, C. E.; Molina, M. J. Chemical Kinetics and Photochemical Data for Use in Stratospheric Modeling, NASA, Evaluation No. 11, 1994.
(34) Wallington, T. J.; Dagaut, P.; Kurylo, M. J. *J. Photochem. Photobiol. A: Chem.* **1988**, *42*, 173.
(35) Adachi, H.; Basco, N.; James, D. G. L. *Int. J. Chem. Kinet.* **1979**, *11*, 1211.
(36) Bauer, D.; Crowley, J. N.; Moortgat, G. K. *J. Photochem. Photobiol. A: Chem.* **1992**, *65*, 329.
(37) Anastasi, C.; Waddington, D. J.; Woolley, A. *J. Chem. Soc., Faraday Trans. 1* **1983**, *79*, 505.
(38) Cattell, F. C.; Cavanagh, J.; Cox, R. A.; Jenkin, M. E. *J. Chem. Soc., Faraday Trans. 2* **1986**, *82*, 1999.
(39) Fenter, F. F.; Catoire, V.; Lesclaux, R.; Lightfoot, P. D. *J. Phys. Chem.* **1993**, *97*, 3530.
(40) Adachi, H.; Basco, N.; James, D. G. L. *Int. J. Chem. Kinet.* **1979**, *11*, 995.
(41) Parkes, D. A.; Quinn, C. P. *J. Chem. Soc., Faraday Trans. 1* **1976**, *72*, 1952.
(42) Slagle, I. R.; Feng, Q.; Gutman, D. *J. Phys. Chem.* **1984**, *88*, 3648.
(43) Kaiser, E. W.; Rimai, L.; Wallington, T. J. *J. Phys. Chem.* **1989**, *93*, 4094.
(44) Munk, J.; Pagsberg, P.; Ratajczak, E.; Sillesen, A. *J. Phys. Chem.* **1986**, *90*, 2752.
(45) Wallington, T. J.; Andino, J. M.; Kaiser, E. W.; Japar, S. M. *Int. J. Chem. Kinet.* **1989**, *21*, 1113.
(46) Arthur, N. L. *J. Chem. Soc., Faraday Trans. 2* **1986**, *82*, 1057.
(47) Anastasi, C.; Arthur, N. L. *J. Chem. Soc., Faraday Trans. 2* **1987**, *83*, 277.
(48) Plumb, I. C.; Ryan, K. R. *Int. J. Chem. Kinet.* **1981**, *13*, 1011.
(49) Wagner, A. F.; Slagle, I. R.; Sarzynski, D.; Gutman, D. *J. Phys. Chem.* **1990**, *94*, 1853.
(50) Certain commercial materials and equipment are identified in this paper in order to adequately specify the experimental procedure. Such identification neither implies recommendation nor endorsement by the National Institute of Standards and Technology, nor does it imply that the material or equipment identified is the best available for the purpose.
(51) Seigman, A. E. *Lasers*; University Science Books: Mills Valley, CA, 1986.
(52) The operating characteristics and design of a similar photomultiplier base circuit is described in: Beck, G. *Rev. Sci. Instrum.* **1976**, *47*, 537. Our design differs slightly in that it uses Zener diodes to clamp each amplification stage to a fixed voltage differential.
(53) Maric, D.; Burrows, J. P.; Meller, R.; Moortgat, G. K. *J. Photochem. Photobiol. A: Chem.* **1993**, *70*, 205.
(54) Wendt, H. R.; Hunziker, H. E. *J. Chem. Phys.* **1984**, *81*, 717.
(55) Rao, C. N. R.; Goldman, G. K.; Balasubramanian, A. *Can. J. Chem.* **1960**, *38*, 2508.
(56) McQuarrie, D. A. *Statistical Mechanics*; Harper & Row: New York, 1975.
(57) Robinson, P. J.; Holbrook, K. A. *Unimolecular Reactions*; Wiley-Interscience: London, 1972.